

A Candidate Dual QSO at Cosmic Noon

EILAT GLIKMAN,¹ RACHEL LANGGIN,^{2,3} MAKOTO A. JOHNSTONE,¹ ILSANG YOON,⁴ JULIA M. COMERFORD,⁵
BROOKE D. SIMMONS,⁶ HANNAH STACEY,⁷ MARK LACY,⁴ AND JOHN M. O'MEARA^{8,9}

¹*Department of Physics, Middlebury College, Middlebury, VT 05753, USA*

²*Department of Astrophysics, Haverford College, Haverford, PA 19041, USA*

³*Bryn Mawr College, Bryn Mawr, PA 19010, USA*

⁴*National Radio Astronomy Observatory, 520 Edgemont Road, Charlottesville, VA 22903, USA*

⁵*Department of Astrophysical and Planetary Sciences, University of Colorado, Boulder, CO 80309, USA*

⁶*Department of Physics, Lancaster University, Bailrigg, Lancaster LA1 4YB, UK*

⁷*Max Planck Institute for Astrophysics, Karl-Schwarzschild Str 1, D-85748 Garching bei München, Germany*

⁸*Department of Physics, Saint Michael's College, One Winooski Park, Colchester, VT, 05439, USA*

⁹*W.M. Keck Observatory 65-1120 Mamalahoa Highway, Kamuela, HI 96743, USA*

ABSTRACT

We report the discovery of a candidate dual QSO at $z=1.889$, a redshift that is in the era known as “cosmic noon” where most of the Universe’s black hole and stellar mass growth occurred. The source was identified in *Hubble* Space Telescope WFC3/IR images of a dust-reddened QSO that showed two closely-separated point sources at a projected distance of $0''.26$, or 2.2 kpc. This red QSO was targeted for imaging to explore whether red QSOs are hosted by merging galaxies. We subsequently obtained a spatially-resolved STIS spectrum of the system, covering the visible spectral range, and verifying the presence of two distinct QSO components. We also obtained high-resolution radio continuum observations with the VLBA at 1.4 GHz (21-cm L band) and found two sources coincident with the optical positions. The sources have similar black hole masses, bolometric luminosities, and radio loudness parameters. However, their colors and reddenings differ significantly. The redder QSO has a higher Eddington ratio, consistent with previous findings. We consider the possibility of gravitational lensing and find that it would require extreme and unlikely conditions. If confirmed as a bona-fide dual QSO, this system would link dust-reddening to galaxy and supermassive black hole mergers, opening up a new population in which to search for samples of dual AGN.

Keywords: Quasars (1319), Double quasars (406)

1. INTRODUCTION

The next generation gravitational wave experiment, LISA, will detect the signal from the coalescence of supermassive black holes (SMBHs) in the $10^5 - 10^7 M_\odot$ range. Since every large galaxy hosts a nuclear SMBH, understanding the black hole merger process into the supermassive regime is essential for a full picture of galaxy evolution. Galaxy mergers have also been invoked to explain the many scaling relations seen between galaxies and their nuclear supermassive black holes (SMBHs) suggesting a co-evolution between the two systems (Magorrian et al. 1998; Gebhardt et al. 2000; Marconi & Hunt 2003). In addition, gas-rich (i.e., “wet”) mergers are understood to trigger the most luminous QSOs through the funneling of gas and dust into the nucleus fueling accretion onto the SMBHs, which are also being brought together by the merger (Sanders

et al. 1988). It is expected, therefore, that at some point during this process both SMBHs will be simultaneously active and therefore discoverable as a pair of active galactic nuclei (AGNs).

While theoretical investigations into the physics of SMBH binaries (e.g., mass ratio, coalescence time scale, AGN activity) have been making steady progress, observational constraints are still lacking due to the small numbers of confirmed dual AGNs. These simulations do find that late-stage major mergers are the most likely to produce dual AGNs (i.e., separations ≤ 10 kpc; Van Wassenhove et al. 2012; Blecha et al. 2013; Steinborn et al. 2016) suggesting that those are the best systems in which to search.

Dust-reddened (or, red) QSOs, represent a short-lived phase of QSO evolution driven by the “wet” merger scenario described above. During such a merger, much of

the black hole growth occurs in a heavily enshrouded environment followed by a relatively brief transitional phase in which the obscuring dust is cleared by outflows and radiation-driven winds and is seen as a moderately reddened, Type 1, luminous QSO. After feedback processes clear the dust, the canonical blue QSO shines through and dominates (Sanders et al. 1988; Hopkins et al. 2005, 2008). Objects in the transitional phase, i.e., moderately obscured, red QSOs, are farther along the merger timeline, and are thus ideal systems for finding dual AGNs.

Samples of red quasars¹ have been identified through radio plus near-infrared selection (e.g., the FIRST-2MASS, or F2M, red quasar survey; Glikman et al. 2004, 2007, 2012) and, more recently, mid- plus near-infrared selection (e.g., the WISE-2MASS, or W2M, red QSO survey; Glikman et al. 2018, 2022). These red QSO samples span a broad range of redshifts ($0.1 < z < 3$) and reddenings ($0.2 \lesssim E(B - V) \lesssim 1.5$); have very high accretion rates ($L/L_{\text{Edd}} > 0.1$; Kim et al. 2015), sufficient to blow out the obscuring material (Glikman 2017). Their spectra often show broad absorption lines (BALs) that are associated with outflows and feedback (Urrutia et al. 2009). Crucially, *Hubble* Space Telescope (HST) imaging at $z \simeq 0.7$ and $z \simeq 2$ reveals that $\gtrsim 80\%$ of F2M red quasars are hosted by merging galaxies (Urrutia et al. 2008; Glikman et al. 2015) making them more likely to harbor dual AGNs (or, more luminous, dual QSOs).

In this paper, we present the discovery of a candidate dual QSO in HST imaging of a sample of W2M red QSOs from Glikman et al. (2022). The QSO’s redshift of $z \sim 1.9$ probes the epoch of peak AGN and star formation in the universe. Throughout this work we quote magnitudes on the AB system, unless explicitly stated otherwise. When analyzing spectra for extinction properties, we first correct them for Galactic extinction, using the Fitzpatrick (1999) extinction curve. When computing luminosities and any other cosmology-dependent quantities, we use the Λ CDM concordance cosmology: $H_0 = 70 \text{ km s}^{-1} \text{ Mpc}^{-1}$, $\Omega_M = 0.30$, and $\Omega_\Lambda = 0.70$.

2. SOURCE CHARACTERISTICS

A Cycle 24 HST program imaged the host galaxies of 11 W2M red QSOs (5 QSOs at $z \sim 0.7$ and 6 QSOs $z \sim 2$) to compare with the F2M imaging studies of Urrutia et al. (2008) and Glikman et al. (2015) that fo-

cused on those same redshifts (13 and 11 objects, respectively), using ACS and WFC3/IR, respectively (PID 14706, PI Glikman). The images were observed with a four-point box dither pattern and were reduced using the *Astrodizzle* package with a final pixel scale of $0''.06$. One source, J122016.9+112627.09², appeared as two closely separated point sources (left and middle panels of Figure 1) in both the F105W and F160W filters. The WFC3/IR observations were designed to be identical to those in Glikman et al. (2015), with W2M J1220 having exposure times of 797 s and 1597 s and reaching 3σ surface brightness limits of $23.67 \text{ mag arcsec}^{-2}$ and $23.87 \text{ mag arcsec}^{-2}$ in F105W and F160W, respectively. From the ground, this source appears as a single object with $r = 18.13$ in the Sloan Digital Sky Survey (SDSS) and $H = 16.01$ in 2MASS.

This source possesses an optical spectrum in SDSS and was assigned a redshift of $z = 1.871$ (see §3 for details on the corrected redshift), shown in the right panel of Figure 1. The spectrum is well-fit by a QSO composite spectrum, constructed by combining the UV template of Telfer et al. (2002) with the optical-to-near-infrared template from Glikman et al. (2006) and reddened with the SMC dust law of Gordon & Clayton (1998), by $E(B - V) = 0.246$. We also obtained a near-infrared spectrum with the TripleSpec near-infrared spectrograph (Wilson et al. 2004) on the 200-inch Hale telescope at the Palomar Observatory, also shown in Figure 1. The Balmer lines are shifted into the atmospheric absorption bands and cannot be studied from the ground. Due to the seeing-limited resolution of $\sim 1''$, this optical-through-near-infrared spectrum represents the combined light of both components and is therefore not well-fit by a single reddened QSO across the full wavelength range.

W2M J1220 is also detected in the FIRST survey with an integrated flux density of $F_{\text{int},20\text{cm}} = 2.33 \text{ mJy}$ ($F_{\text{pk},20\text{cm}} = 1.50 \text{ mJy/beam}$), which corresponds to a total radio power of $P_{1.4\text{GHz}} = 5.7 \times 10^{25} \text{ W Hz}^{-1}$. Table 1 lists the optical through near-infrared photometry for this source.

2.1. Morphological modeling

To determine the separation of the two sources and measure their respective magnitudes we modeled the WFC3/IR images in both filters using Galfit (Peng et al. 2002). We used a point spread function (PSF) constructed by combining a few dozen bright stars in each HST filter from observations that used the same dither pattern following the same procedure as in Glikman

¹ In this letter, we adopt the canonical nomenclature that distinguishes quasars, radio-detected luminous AGN whose radio emission is essential to their selection, from QSOs, the overall class of luminous AGN.

² Hereafter, W2M J1220

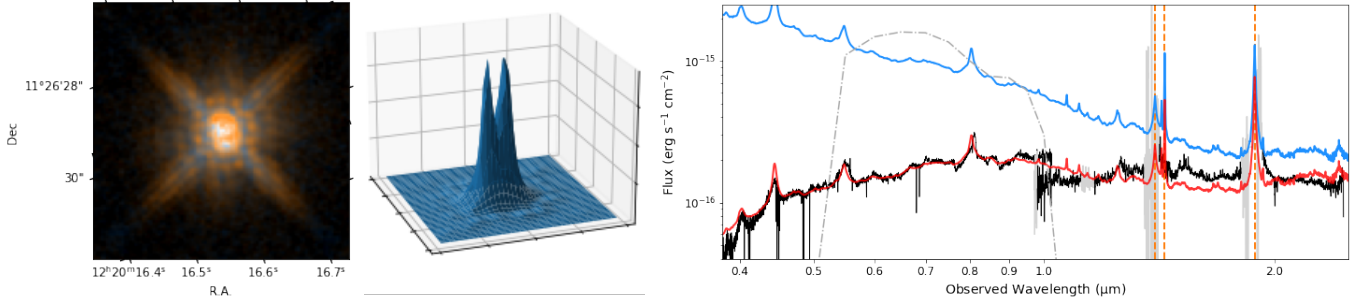


Figure 1. *Left* – Color combined WFC3/IR image showing the presence of two closely-separated central peaks. The red layer is the F160W image, the green layer is an average of the F160W and F105W images, and the blue layer is the F105W image. *Middle* – Surface plot of the image counts in the F160W image where two distinct sources are visible. *Right* – Optical through near-infrared spectrum of W2M1220+1126 (black line). A reddened QSO template, made out of the UV composite QSO template of Telfer et al. (2002) combined with the optical-to-near-infrared composite spectrum from Glikman et al. (2006), with $E(B - V) = 0.246$ is overplotted with a red line and an unreddened QSO template is shown in blue. We see that the Balmer lines are shifted into the atmospheric absorption bands. The STIS G750L transmission curve used in this work is shown with a gray dot-dash curve.

Table 1. Photometric properties of F2M J1220

Band	AB mag
g	19.07±0.01
r	18.130± 0.008
i	17.452±0.007
z	17.12±0.01
J	16.44±0.07
H	16.01±0.06
K	15.67±0.06
Northern Component ^a	
F105W	18.020±0.003
F160W	16.9739±0.0002
Southern Component ^a	
F105W	17.411±0.002
F160W	16.8656±0.0004

^aThe magnitudes reported from the HST images are based on the PSF components determined by Galfit as described in §2.1.

et al. (2015) using stars whose images were obtained within 12 months of W2M 1220. The stars used to construct the PSF were chosen to lie in the central region of the WFC3/IR detector to minimize distortion effects. All archival observations were re-reduced using the same *Astrodizzle* parameters as W2M 1220. When fitting, all parameters were allowed to be free in both filter images, which produced the best fits (i.e., smallest χ^2_ν) and cleanest residuals. Attempts at fixing

the positions of the F160W and F105W components to each other resulted in poorer fits and yielded residuals with strong negative/positive flux asymmetries.

We first fit a model consisting of two PSFs and a background sky component. While both sources are consistent with a point spread function, the residual image showed excess flux in need of additional model components. We added a Sérsic component to the model resulting in a better fit, verified by an F-test whose probability was consistent with 0, strongly suggesting that we can reject the null hypothesis. However, the best-fit Sérsic component, situated next to the southern PSF, had an effective radius, R_e , of 0.06 pixels, which is not physically meaningful. Although the addition of this Sérsic component improved the fit statistic and accounted for flux not captured by the PSFs, it is unclear how much of this added component was accounting for PSF mismatches³. Because the added Sérsic did not model the extended emission seen in the residual image to the east of the two PSFs, we added a second Sérsic component, which does account for this excess flux and whose inclusion is supported by an F-test with probability consistent with 0.

The best-fit Galfit model therefore is composed of two PSFs and two Sérsic components. The locations of the PSFs, in both filters, indicate a projected separation of $0.2680 \pm 0.0003''$, which corresponds to ~ 2.2 kpc at the QSO's redshift. Figure 2 shows the residual images from this fit where different model components have been sub-

³ Extensive investigation into the PSF subtraction did not reveal any systematic effects when fit to archival point sources located at the same pixel position as W2M 1220. However, we find that the PSF is not able to capture all the flux from very bright point sources resulting in significant, yet symmetric residuals.

tracted from the data. We mark in the rightmost panel the positions of the four model components. Table 2 lists the best-fit parameters for this model, noting that the first Sérsic component may not represent a physically meaningful model.

2.2. *HST* follow-up with STIS

We obtained STIS spatially-resolved spectroscopy in the G750L mode covering a wavelength range from 5240–10270 Å (dot-dash line in Figure 1; Cycle 29, PID 16794). The $52'' \times 0.2''$ slit was oriented at a position angle of 177.286° to capture both components in a single observation. The STIS CCD has a plate scale of $0.05078''/\text{pixel}$ such that the two components are separated by ~ 5 pixels. The standard STIS reduction pipeline was used to remove detector signatures and defringe the spectra using the STIS tools `defringe.defringe` command to remove the fringing pattern.

We use the `x1d` routine to extract each spectrum, adjusting the parameters to minimize overlap between the two. We constrain the search region for finding a peak in the extraction profile by setting `MAXSRCH` to 1.5 for each source and `A2CENTER` to 506 and 511 pixels, respectively. We set the extraction box size to 3 pixels and use a 10 pixel offset from the peak, which is far from both source profiles, for the background subtraction region. Two distinct spectra were extracted at 511.383 pixels and 506.324 pixels, respectively.

To evaluate the impact of blending on our spectral extraction, we sum the cosmic-ray cleaned, normalized, and defringed science spectrum along the wavelength axis and plot the spatial profile of the two spectra in Figure 3. We fit two Gaussian distributions to this summed profile, keeping the width of the Gaussians tied to each other, and fixing the centers to the positions found by `x1d`. The extracted region for each spectrum is shown in light and dark shaded pink. Using the best-fit σ of 1.04 pixels, we calculate that the southern spectrum overlaps the northern spectrum by $\sim 0.6\%$, ensuring that the individual spectra are not contaminated by blending. We also determine that the 3-pixel aperture loses 14.8% of the total flux. We correct the fluxes of our spectra by this amount.

Figure 4, left, shows the resultant extracted spectra for both QSO components. The Mg II line that is seen in the SDSS spectrum (Fig. 1) is visible in both the southern and northern components at 2800\AA . However, the C III] line at $\sim 2000\text{\AA}$ is only seen in the southern component, where the signal-to-noise ratio is sufficiently high. The two spectra have different continuum shapes and the redder color of the northern component seen

in the WFC3/IR image is apparent in the spectrum as well.

2.3. VLBA Imaging

W2M J1220 is detected in the FIRST catalog (Becker et al. 2003) with a 20 cm integrated flux density of 2.33 mJy. The peak flux density is 1.50 mJy/beam with an rms of 0.146 mJy/beam. The source’s deconvolved major and minor axes are $5.57''$ and $2.26''$, respectively, indicating that the image is slightly resolved⁴.

Aiming to detect two distinct radio components at their optical positions, we obtained 257 minutes of on-source integration with the Very Long Baseline Array (VLBA) split into two equal-length dual polarization observations on 19 August 2021 and 03 December 2021 in the L-band (1.4 GHz or 20 cm). We used J1218+1105 as a phase calibrator, which we measure to have an integrated flux density of 0.177 Jy in L-band located only 0.58 deg away from our target.

The observations were flagged, calibrated, cleaned, and imaged with the Common Astronomy Software Applications (CASA; CASA Team et al. 2022) package Version 6.5, following the approach described in VLBA Science Memo #38 (Linford 2022). Fort Davis (FD) was selected as the reference antenna. To ensure that the amplitude scaling accounted for the wide bandpass, the task `ACCOR` was run twice – first for the initial calibrations and again after the bandpass correction. A phase-referenced (Stokes I) image of the target was produced by applying the `TCLEAN` task with natural weighting. The final calibrated image spans $320 \times 0.001''$ along each axis with an rms noise level of 0.017 mJy and is shown in Figure 5.

The calibrated VLBA image shows two distinct point sources oriented at a position angle of 172.205° with a separation of $0.26''$ (2.2 kpc). We performed 2D Gaussian fitting on each source with `CASAvviewer` and found that the northern source has an integrated flux density of 0.502 ± 0.066 mJy and a peak flux density of 0.165 ± 0.016 mJy/beam. The deconvolved major and minor axes are $0.0234''$ and $0.0087''$. The southern source has an integrated flux density of 0.330 ± 0.044 mJy, a peak flux density of 0.146 ± 0.014 mJy/beam, and deconvolved major and minor axes of $0.0166''$ and $0.0072''$. In both sources, the major axis is slightly larger than the CLEAN beam which has FWHM of $0.01''$ along both axes.

We overlay in contours the HST WFC3/IR F160W fluxes. The two VLBA point sources and their position angles are consistent with the HST position, though out-

⁴ The FIRST survey has an angular resolution of $5''$.

Table 2. Galfit parameters

Component	F160W ($\chi^2_\nu = 58.2$)					F105W ($\chi^2_\nu = 28.8$)				
	R.A. ^a	Decl. ^a	Mag	n	R_e	R.A. ^a	Decl. ^a	Mag	n	R_e
	(J2000)	(J2000)	(mag)		(kpc)	(J2000)	(J2000)	(mag)		(kpc)
North PSF	+0.8800	+0.2805	16.97	+0.8783	+0.2875	18.02
South PSF	+0.8785	+0.0097	16.87	+0.8781	+0.0232	17.41
Sérsic (central)	+0.8922	+0.0668	20.31	1.32 ± 6.21	0.03 ± 0.23	+0.8926	+0.0471	21.00	1.76^b	0.02^b
Sérsic (eastern)	+0.9379	+0.1756	20.89	1.94^b	1.5^b	+0.9383	+0.1469	20.31	1.50 ± 0.37	1.01 ± 0.04

^aThe positions reported are shifts in seconds with respect to R.A. 12:20:16 and shifts in arcseconds with respect to Decl. +11:26:28.

^bThese parameters are flagged by Galfit as being outside the range of acceptable values. However, the fit resulted in an acceptable χ^2_ν enabling a capture of the residual flux in the components. We do not report errors for these parameters.

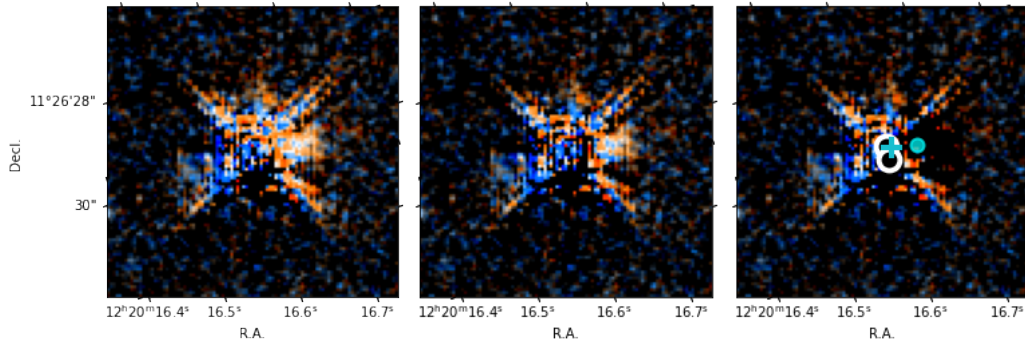


Figure 2. Color combined residual images from the best-fit Galfit model, as described in Table 2. *Left* – HST WFC3/IR image with just the two PSF components subtracted. *Middle* – Both PSF components and central Sérsic component subtracted; bright extended emission is seen to the east. *Right* – Full residual with all model components subtracted. In this frame, the best-fit model parameters are marked. White circles are at the PSF positions. The cyan cross is the central Sérsic parameter located slightly to the east of the southern PSF. The cyan circle is the position of the Sérsic component that best-fits the extended emission farther to the east.

side the $0''.03$ Gaia-based astrometric errors, confirming their associations as the two components of W2M J1220.

3. RESULTS

With our near-infrared imaging, spatially-resolved optical spectroscopy, and 20 cm radio imaging in hand, we are able to analyze the properties of the individual QSO components. We noticed that the SDSS-assigned redshift of $z = 1.871$ was based on the C IV line, which did not align with the Mg II line in the STIS spectra. Since C IV is known to be blueshifted relative to QSOs’ systemic redshifts (Richards et al. 2011), we update the source redshift to $z = 1.889$ based on the Mg II line center derived from these new observations. We fit a reddened QSO template to each spectrum and find that the southern source has $E(B - V) = 0.179 \pm 0.001$ while the northern source has $E(B - V) = 0.458 \pm 0.009$. These fits are shown with a pink line in Figure 4. We

correct the observed F160W photometry, corresponding to rest-frame 5320\AA , by these extinction values and, applying a bolometric correction of 9.2 (Richards et al. 2006), compute $L_{\text{bol,south}} = 3.06 \times 10^{44} \text{ erg s}^{-1}$ and $L_{\text{bol,north}} = 4.84 \times 10^{44} \text{ erg s}^{-1}$. This means that the northern source, which appears fainter, is intrinsically more luminous after correcting for its substantially higher amount of extinction. We note that the intrinsically more luminous component coincides with the brighter radio source.

We fit a Gaussian profile to the Mg II line in both spectra to measure the v_{FWHM} values as $2830 \pm 650 \text{ km s}^{-1}$ and $3920 \pm 260 \text{ km s}^{-1}$ in the northern and southern sources, respectively. The errors are computed by perturbing the best fit model using the spectrum’s error array and re-fitting 10,000 times. We compute the standard deviation of the Gaussian σ parameter found in each fit iteration, shown in the right panels Figure 4.

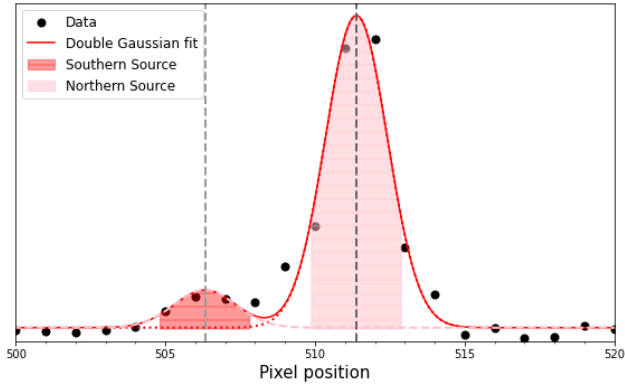


Figure 3. Spatial profile of the source spectrum collapsed along the x-direction. Black points are the summed counts at each spatial pixel position, and the red line is a double Gaussian fit to the data. The shaded areas represent our $3''$ extraction regions, chosen to minimize blending. Two distinct peaks are shown with the southern spectrum overlapping the northern spectrum by $\sim 0.6\%$.

For the two QSOs, we apply the single-epoch virial black hole mass estimator (M_{BH}) following the formalism of Shen & Liu (2012),

$$\log\left(\frac{M_{\text{BH, vir}}}{M_{\odot}}\right) = a + b \log\left(\frac{L_{3000}}{10^{44} \text{ erg/s}}\right) + c \log\left(\frac{v_{\text{FWHM}}}{\text{km/s}}\right), \quad (1)$$

adopting the values $a = 0.740$, $b = 0.620$, $c = 2.00$ for single-epoch measurements of $\text{FWHM}_{\text{MgII}}$ and L_{3000} , based on the calibration of Shen et al. (2011). For this calculation, we estimate L_{3000} two different ways. We measure it directly from the STIS spectra by applying an aperture correction to the observed flux, and de-reddening each spectrum. We then apply an artificial 30 \AA -wide box-car filter centered on 3000 \AA to measure the source flux, from which we determine luminosity. The second method starts with the F160W source magnitudes (Table 1), which are far less sensitive to uncertainties in $E(B - V)$. We de-redden these magnitudes and use spectrophotometry to scale a QSO composite template to match the F160W flux. From the scaled template, we measure the 3000 \AA flux using the box-car filter as in the previous method. This results in a range of black hole masses, listed in Table 3. The BH masses differ for each method by $\lesssim 0.5$ dex but are extremely similar ($\lesssim 0.2$ dex) between the two components. These masses are at the high end of the range accessible to LISA.

Combining M_{BH} and L_{bol} allows us to estimate the Eddington ratio. We find that the more obscured northern source has $L/L_{\text{Edd}} \simeq 0.1 - 0.3$, while the less obscured, southern source has $L/L_{\text{Edd}} \simeq 0.04 - 0.1$. This is consistent with findings that red QSOs have higher

accretion rates than their unobscured counterparts (Urrutia et al. 2012; Kim et al. 2015).

From the definition, $R \equiv f(1.4 \text{ GHz})/f(B)$, we calculated the radio loudness parameter of the two sources. The optical flux is determined by the method described above, where the QSO template, scaled to the de-reddened F160W flux, is passed through a Johnson B filter curve. The radio flux is not K-corrected, given that the radio spectral index for each source is not known. We find that both sources have nearly identical R values, at the boundary of the radio-quiet regime⁵, with $R_{\text{north}} \approx 0.46$ and $R_{\text{south}} \approx 0.48$. Table 3 lists all the derived properties for the two QSOs in this dual system.

4. DISCUSSION

The confirmation of two distinct QSO spectra, at the same redshift, separated by $0''.26$, and coincident with two compact radio sources provides strong evidence that W2M J1220 is a dual QSO. Most of the known and confirmed dual AGNs are at low redshifts ($z < 0.7$; e.g. Koss et al. 2012; Comerford et al. 2012; Müller-Sánchez et al. 2015; Fu et al. 2015; Rubinur et al. 2019), which is not yet probing the epoch of peak QSO activity in the universe ($z \simeq 2$; Madau & Dickinson 2014) when merger rates were significantly higher (Conselice et al. 2003; Rodriguez-Gomez et al. 2015). Therefore, the identification of a dual QSO system at this epoch is noteworthy, especially given that red QSOs are predominantly found in merging hosts.

W2M J1220 is comparable to LBQS 0103–2753 (Shields et al. 2012), which is a confirmed dual QSO, separated by $0''.3$, at $z = 0.858$. LBQS 0103–2753 was identified in HST imaging and verified with a STIS spectrum, similar to W2M J1220. Deep HST imaging of LBQS 0103–2753 reveals tidal features and morphological evidence of a recent merger. The WFC3/IR imaging for W2M J1220 is not deep enough to show these features. The two-component spectra of LBQS 0103–2753 are quite distinct, with one of the components showing BAL features indicative of outflows. There is also a velocity offset of $\sim 1500 \text{ km s}^{-1}$ between the two components. Although the black hole masses of LBQS 0103–2753 are $\sim 1 - 1.5$ orders of magnitude higher than W2M J1220, they are similar to each other (both have $M_{\text{BH}} \sim 10^{8.5-9} M_{\odot}$).

In the cosmic noon era ($z \sim 2 - 3$), Shen et al. (2021) report two dual QSO candidates using the novel

⁵ Objects with $R > 2$ are categorized as “radio-loud”, while objects are generally considered “radio-quiet” when $R < 0.5$. Radio-intermediate sources are those that fit neither category $0.5 < R < 2$ (Stocke et al. 1992).

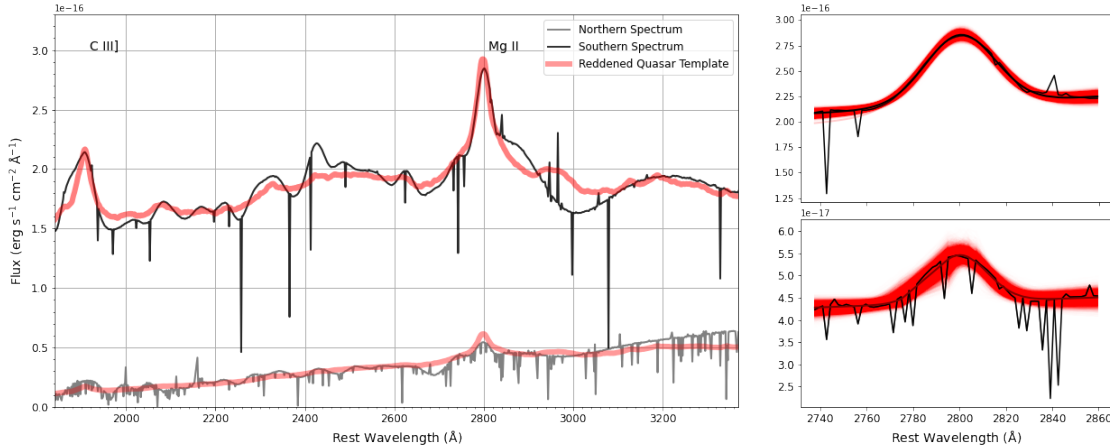


Figure 4. *Left* – Individual spectra of the two QSO components plotted at rest wavelengths. The pink curves represent the best-fit reddened QSO template. The northern source (gray line) is reddened by $E(B - V) = 0.432$ while the southern source (black line) is reddened by $E(B - V) = 0.184$. Mg II and C III] lines are labeled. *Right* – Gaussian fits to the Mg II emission line in the southern (top) and northern (bottom) spectra showing 10,000 iterations determined by perturbing the best-fit line using the error arrays. The range of fits reflects the uncertainty in the derived Gaussian parameters.

Table 3. Individual QSO characteristics

Source	R.A. ^a (J2000)	Decl. ^a (J2000)	$E(B - V)$ (mag)	v_{FWHM} (km s ⁻¹)	$\log M_{\text{BH}}^b$ (M_{\odot})	$\log L_{\text{bol}}$ (erg s ⁻¹)	L/L_{Edd}	$S_{\text{pk},20\text{cm}}$ (mJy)	R
North	12:20:16.87176	+11:26:28.344	0.458 ± 0.009	3140 ± 800	$(7.2 - 7.7) \pm 0.2$	44.76	$0.08 - 0.22$	0.502 ± 0.066	0.460
South	12:20:16.87420	+11:26:28.082	0.179 ± 0.001	3800 ± 230	$(7.40 - 7.70) \pm 0.04$	44.46	$0.05 - 0.1$	0.330 ± 0.044	0.478

^aThe celestial coordinate positions are from the VLBA data and have the uncertainties $\delta_{\text{R.A.}} = 0.00003\text{s}$ and $\delta_{\text{Decl.}} = 0.001''$.

^bThe range of $\log M_{\text{BH}}$ is based on the two methods for estimating L_{3000} while the quoted uncertainties are based on the propagation of the v_{FWHM} uncertainties and are therefore lower limits.

technique of ‘varstrometry’ which identifies sources with high astrometric variability in Gaia suggestive of two distinct, closely-spaced sources with randomly varying fluxes (Hwang et al. 2020). One source, J0841+4825, is at $z = 2.95$ and is separated by $0''.46$, though its ground-based spatially-resolved spectroscopy shows highly similar spectra which could be explained by gravitational lensing. Both components of J0749+2255, at $z = 2.17$ and also separated by $0''.46$, are detected by VLBA observations at 15 GHz, has a spatially resolved STIS spectrum, and HST imaging showing merger signatures in the host, putting this system on solid footing for a dual QSO (Chen et al. 2023). There are 45 additional varstrometry-selected dual QSO candidates extending out to $z \simeq 3$ awaiting confirmation (Chen et al. 2022).

The gravitational lens PSJ1721+8842, initially thought to be a quadruple lens at $z = 2.37$, was analyzed by

Mangat et al. (2021) to re-interpret the system as two QSOs that are lensed to form four point source images based on HST optical and IR observations as well as VLA observations.

Yue et al. (2021) report a candidate QSO pair at $z = 5.66$ separated by $1''.24$, or 7.3 kpc. Spatially resolved spectroscopy reveal two spectra with similar line characteristics but different reddenings, as in W2M J1220.

4.1. Lensing considerations

Some of the properties between the two components of W2M J1220, such as the derived black hole masses, radio loudness parameters, as well as near-identical emission line centers and profile shapes, may be explained by gravitational lensing. Here we consider that possibility.

Figure 6 shows the ratio of the northern to southern spectrum, with the ratio of the best-fit reddened templates (pink curves in Figure 4) over-plotted. While

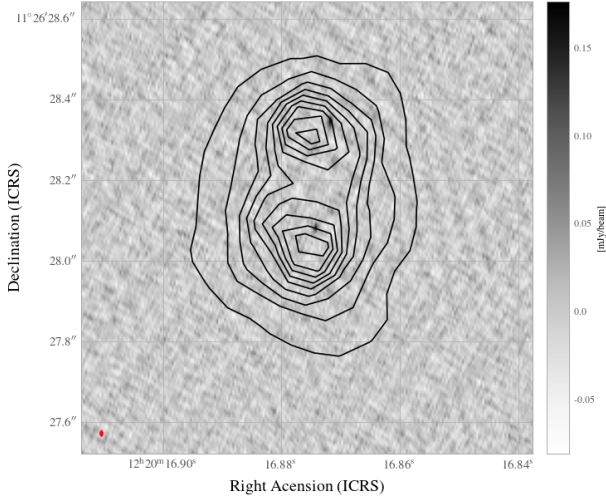


Figure 5. Calibrated and cleaned image of VLBA L-band observations of W2M J1220 produced with CASA. Overplotted contours indicate the flux from the WFC3/IR F160W image at 5σ levels. Two point sources are detected at the HST position with a separation of $0''.26$ and a position angle of 172.205° . Beam size of $0''.005$ is shown in red in the bottom left.

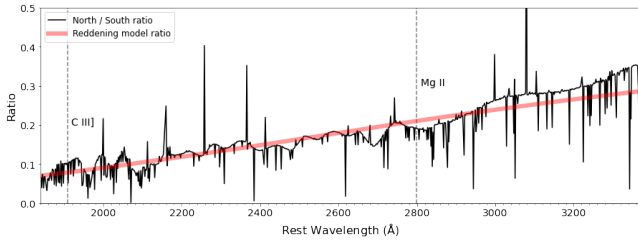


Figure 6. Flux ratio of the northern to southern spectra showing the disappearance of the C IV and Mg II emission lines (vertical dashed lines), motivating an exploration of gravitational lensing as the cause for the pair of QSO images. The pink line represents a ratio of the best-fit reddening curves shown in Figure 4.

the C IV and Mg II emission lines, marked by vertical dashed lines, disappear, the shape of the ratio is broadly consistent with the difference in reddening. The undulating features that deviate from a QSO template seen in both the ratio spectrum and in the southern component are not consistent with known QSO spectral features, such as iron emission in the ultraviolet (UV; Vestergaard & Wilkes 2001).

With a separation of $0''.26$, corresponding to an Einstein radius of $0''.13$, W2M J1220 would be the

most closely-separated lensed QSO known⁶. Such small-separation lenses (on the order of ~ 100 milli-arcseconds or, so-called, milli-lenses; Frey et al. 2010; Spingola et al. 2019; Casadio et al. 2021) are rare and have been difficult to find, but probe supermassive ($10^6 - 10^9$) compact objects as putative lenses. Recent systematic searches using VLBA data have resulted in few viable candidates. This is because a lens with an unusually high surface density is needed to yield such small separations.

We explore the range of possible lens masses that could result in a separation of $0''.26$ as a function of redshift to determine the plausibility of lensing in W2M1220. We employ the relation among distances, lens mass, and source separation, and a point mass lens,

$$M(\theta_E) = \left(\frac{c^2}{4G} \right) \theta_E^2 \left(\frac{D_d D_s}{D_{ds}} \right), \quad (2)$$

and for a singular isothermal sphere (SIS) mass model,

$$M(\theta_E) = \frac{\sigma_v^2 R}{G} \quad \text{with} \quad \sigma_v = c \sqrt{\frac{\theta_E D_s}{4\pi D_{ds}}}. \quad (3)$$

Here, $M(\theta_E)$ is the mass enclosed within the angular radius θ_E , D_d and D_s are the angular diameter distance to the lens, source, respectively, and D_{ds} is the angular diameter distance between the lens and source. Given the redshift of W2M J1220, D_s is known we can compute $M(\theta_E)$ as a function of lens redshift. We find that even the smallest lens masses, residing at $z \sim 0.4 - 0.6$, would require $> 10^9 M_\odot$ to be confined to the innermost kpc².

Assuming lensing as a possibility, we model the system with GRAVLENS (Keeton 2001) and determine the lens position that would yield the two VLBA positions finding that a lens would need to be situated $0''.021695$ to the west and $0''.159543$ to the south of the northern source. An attempt to fix a Sérsic component at this position relative to fixed PSF components in our morphological fitting (§2) resulted in failure of Galfit to converge. In fact, the central Sérsic component found by Galfit, while possessing unphysical properties, is situated to the *east* of both PSF components.

Identifying intrinsic differences, such as in the spectral slope, between the two QSOs would rule out lensing. The $E(B - V)$ values that we find are determined with respect to a composite QSO spectrum that has a spectral slope of $\alpha_\nu = -0.47$ at $\lambda < 5000$. We vary the slope of the QSO template (following Section

⁶ J0439+1634 has a separation of $0''.2$ (Fan et al. 2019). This source is of the rare class of “naked” cusp lenses involving three images, which is ruled out for our system by the VLBA image. B0218+357, with a separation of $0''.34$ is currently the next most closely-separated lens (Patnaik et al. 1993).

5.3 of Glikman et al. 2007) and recomputed $E(B - V)$ for a template with $\alpha_\nu = -0.25$ (a bluer slope) and $\alpha_\nu = -0.76$ (a redder slope), which represent the range intrinsic to unreddened QSOs (Richards et al. 2003). While the bluer template does yield slightly higher values by $\Delta E(B - V) \sim 0.02$ (and vice-versa for the redder template, yielding lower values by $\Delta E(B - V) \sim 0.03$), the differences are not sufficient to account for the difference in $E(B - V)$ between the two sources as seen in the continuum fits (Figure 4), the flux ratios (Figure 6) and the $F105W - F160W$ colors. We therefore cannot attribute the different reddenings to intrinsic differences in spectral slopes between the two spectra and the best explanation for the $E(B - V)$ values is different amounts of dust reddening along the two lines of sight.

To achieve the observed amount of reddening would require a lensing galaxy with a significant amount of gas and dust. While we cannot rule out lensing with this spectral slope investigation, it does rule out the exotic possibility that the lens might be a freely floating SMBH.

Finally, the similarities between the black hole properties in W2M J1220 are seen in previously confirmed dual QSOs, such as LBQS 0103–2753 (Shields et al. 2012). Simulations of SMBH binaries predict major mergers more often produce dual AGNs with similar BH masses (Blecha et al. 2013; Steinborn et al. 2016). And, since red QSOs are known to be associated with major mergers, this discovery may reflect a selection effect towards similar mass BHs.

The similarity in radio loudness may reflect the enhanced low-level radio emission seen in W2M red QSOs, which has been interpreted as coming from either a dusty wind or nascent jets (Glikman et al. 2022). Likewise, the differences between the two QSOs, such as the higher accretion rate seen in the redder source, is consistent with what has been seen in red QSOs elsewhere (Urrutia et al. 2012; Kim et al. 2015).

Finally, as some gravitational lenses show intervening absorption features in the individual component spectra (e.g., Rubin et al. 2018), which may reveal the putative lens redshift, we explored the absorption features in the STIS spectra and could not identify any evidence for such coherent features. This further weakens the possibility of a gas rich galaxy as a gravitational lens. Therefore, although we cannot definitively rule it out, we consider lensing to be the less likely explanation for this system.

One way to rule out lensing would be to obtain deeper imaging with HST that may reveal evidence of a merging system, as is seen in the dual QSO found by Chen et al. (2023). Another way would be to measure the flux

densities at other radio frequencies and compare their radio spectral indices which, if different for each source, would also rule out lensing. And, if a lens is responsible, its nature as highly compact and with extreme dust gradients, is worthy of its own study.

4.2. dual statistics for red QSOs

The serendipitous discovery of a QSO pair in HST imaging of a red QSO raises the question of their frequency compared to unreddened QSOs. Shen et al. (2023) investigate statistically the incidence of QSO pairs using Gaia detections of known SDSS QSOs with $L_{\text{bol}} > 10^{45.8} \text{ erg s}^{-1}$ at $1.5 < z < 3.5$ with separations of $0''.4 - 3''$ and find an integrated pair fraction of $\sim 6 \times 10^{-4}$. Assuming this fraction is constant at the $0''.26$ separation of W2M 1220 and is a factor of ~ 10 higher given its lower luminosity ($L_{\text{bol}} \sim 10^{44.8} \text{ erg s}^{-1}$), the pair fraction is estimated to be $\sim 10^{-3}$ (Shen et al. 2023). However, only 17 red QSOs have been imaged with HST at $z \sim 2$ (11 F2M quasars reported in Glikman et al. 2015, and 6 W2M QSOs which include W2M 1220). This fraction of 0.06 (1/17) would be an order of magnitude higher than that found for the luminous, unobscured QSOs investigated in Shen et al. (2023). Given that red QSOs are known to be hosted by major mergers, this population may be the most likely for finding dual QSOs although with only a single system, we cannot draw broad conclusions.

5. CONCLUSIONS

We report the discovery of a dual QSO candidate, separated by $0''.26$ corresponding to 2.2 kpc at $z = 1.889$. The sources are confirmed as QSOs with a spatially-resolved STIS spectrum and high-resolution VLBA imaging at 1.4 GHz which reveal two point sources consistent with the positions in the HST images. The two components are reddened by different amounts of dust-extinction. When corrected for this extinction, the properties of the QSOs are similar, including black hole masses $\sim 10^{7.5} M_\odot$ and radio loudness of ~ 0.5 (though their Eddington ratios differ). These similarities mean we cannot rule out gravitational lensing, though the lens is not detected in the imaging and extended features seen in the HST imaging may indicate merging hosts. The features of these two QSOs are consistent with previous findings in dual AGNs.

A dual QSO discovered at cosmic noon in a survey for red QSOs, which is a population known to be hosted by major mergers, can provide a unique population in which to search for such systems where both black holes are active at the same time. Given that only ~ 30 red quasars have been observed with HST, finding a candi-

date dual QSO in such a small sample suggests an elevated incidence of dual activity in red QSOs. Because W2M J1220 was found serendipitously, a targeted high resolution imaging effort of red QSOs at $z = 2 - 3$ may be the most fruitful place to find dual quasars during a crucial phase of SMBH/Galaxy co-evolution.

We thank Marianne Vestergaard for sharing the Fe UV template which we used to look for features in our spectra. E.G. acknowledges the generous support of the Cottrell Scholar Award through the Research Corporation for Science Advancement. E.G. is grateful to the Mittelman Family Foundation for their generous support. We gratefully acknowledge the National Science Foundation's support of the Keck Northeast Astronomy Consortium's REU program through grant AST-1950797. BDS acknowledges support through a UK Research and Innovation Future Leaders Fellowship [grant number MR/T044136/1].

Some/all of the data presented in this paper were obtained from the Mikulski Archive for Space Tele-

scopes (MAST) at the Space Telescope Science Institute. The specific observations analyzed can be accessed via [10.17909/5ydb-ex84](https://archive.stsci.edu/10.17909/5ydb-ex84) and [10.17909/s2sz-t252](https://archive.stsci.edu/10.17909/s2sz-t252).

This research is based on observations made with the NASA/ESA *Hubble* Space Telescope obtained from the Space Telescope Science Institute, which is operated by the Association of Universities for Research in Astronomy, Inc., under NASA contract NAS 5-26555. These observations are associated with program(s) PID 16794.

The National Radio Astronomy Observatory is a facility of the National Science Foundation operated under cooperative agreement by Associated Universities, Inc. This work made use of the Swinburne University of Technology software correlator (Deller et al. 2011), developed as part of the Australian Major National Research Facilities Programme and operated under licence.

Facilities: HST(STIS), VLBA, SDSS, Palomar(TripleSpec)

Software: astropy (Astropy Collaboration et al. 2013, 2018), astroconda, CASA
[10.17909/5ydb-ex84](https://archive.stsci.edu/10.17909/5ydb-ex84) [10.17909/s2sz-t252](https://archive.stsci.edu/10.17909/s2sz-t252)

REFERENCES

- Astropy Collaboration, Robitaille, T. P., Tollerud, E. J., et al. 2013, *A&A*, 558, A33, doi: [10.1051/0004-6361/201322068](https://doi.org/10.1051/0004-6361/201322068)
- Astropy Collaboration, Price-Whelan, A. M., Sipőcz, B. M., et al. 2018, *AJ*, 156, 123, doi: [10.3847/1538-3881/aabc4f](https://doi.org/10.3847/1538-3881/aabc4f)
- Becker, R. H., Helfand, D. J., White, R. L., Gregg, M. D., & Laurent-Muehleisen, S. A. 2003, *VizieR Online Data Catalog*, VIII/71
- Blecha, L., Loeb, A., & Narayan, R. 2013, *MNRAS*, 429, 2594, doi: [10.1093/mnras/sts533](https://doi.org/10.1093/mnras/sts533)
- CASA Team, Bean, B., Bhatnagar, S., et al. 2022, *PASP*, 134, 114501, doi: [10.1088/1538-3873/ac9642](https://doi.org/10.1088/1538-3873/ac9642)
- Casadio, C., Blinov, D., Readhead, A. C. S., et al. 2021, *MNRAS*, 507, L6, doi: [10.1093/mnrasl/slab082](https://doi.org/10.1093/mnrasl/slab082)
- Chen, Y.-C., Hwang, H.-C., Shen, Y., et al. 2022, *ApJ*, 925, 162, doi: [10.3847/1538-4357/ac401b](https://doi.org/10.3847/1538-4357/ac401b)
- Chen, Y.-C., Liu, X., Foord, A., et al. 2023, *Nature*, 616, 45, doi: [10.1038/s41586-023-05766-6](https://doi.org/10.1038/s41586-023-05766-6)
- Comerford, J. M., Gerke, B. F., Stern, D., et al. 2012, *ApJ*, 753, 42, doi: [10.1088/0004-637X/753/1/42](https://doi.org/10.1088/0004-637X/753/1/42)
- Conselice, C. J., Bershad, M. A., Dickinson, M., & Papovich, C. 2003, *AJ*, 126, 1183, doi: [10.1086/377318](https://doi.org/10.1086/377318)
- Deller, A. T., Briske, W. F., Phillips, C. J., et al. 2011, *PASP*, 123, 275, doi: [10.1086/658907](https://doi.org/10.1086/658907)
- Fan, X., Wang, F., Yang, J., et al. 2019, *ApJL*, 870, L11, doi: [10.3847/2041-8213/aaeffe](https://doi.org/10.3847/2041-8213/aaeffe)
- Fitzpatrick, E. L. 1999, *PASP*, 111, 63, doi: [10.1086/316293](https://doi.org/10.1086/316293)
- Frey, S., Paragi, Z., Campbell, R. M., & Moór, A. 2010, *A&A*, 513, A18, doi: [10.1051/0004-6361/200913864](https://doi.org/10.1051/0004-6361/200913864)
- Fu, H., Wrobel, J. M., Myers, A. D., Djorgovski, S. G., & Yan, L. 2015, *ApJL*, 815, L6, doi: [10.1088/2041-8205/815/1/L6](https://doi.org/10.1088/2041-8205/815/1/L6)
- Gebhardt, K., Bender, R., Bower, G., et al. 2000, *ApJL*, 539, L13, doi: [10.1086/312840](https://doi.org/10.1086/312840)
- Glikman, E. 2017, *Research Notes of the American Astronomical Society*, 1, 48, doi: [10.3847/2515-5172/aaa0c0](https://doi.org/10.3847/2515-5172/aaa0c0)
- Glikman, E., Gregg, M. D., Lacy, M., et al. 2004, *ApJ*, 607, 60
- Glikman, E., Helfand, D. J., & White, R. L. 2006, *ApJ*, 640, 579, doi: [10.1086/500098](https://doi.org/10.1086/500098)
- Glikman, E., Helfand, D. J., White, R. L., et al. 2007, *ApJ*, 667, 673, doi: [10.1086/521073](https://doi.org/10.1086/521073)
- Glikman, E., Simmons, B., Mailly, M., et al. 2015, *ApJ*, 806, 218, doi: [10.1088/0004-637X/806/2/218](https://doi.org/10.1088/0004-637X/806/2/218)
- Glikman, E., Urrutia, T., Lacy, M., et al. 2012, *ApJ*, 757, 51, doi: [10.1088/0004-637X/757/1/51](https://doi.org/10.1088/0004-637X/757/1/51)
- Glikman, E., Lacy, M., LaMassa, S., et al. 2018, *ApJ*, 861, 37, doi: [10.3847/1538-4357/aac5d8](https://doi.org/10.3847/1538-4357/aac5d8)
- . 2022, *ApJ*, 934, 119, doi: [10.3847/1538-4357/ac6bee](https://doi.org/10.3847/1538-4357/ac6bee)
- Gordon, K. D., & Clayton, G. C. 1998, *ApJ*, 500, 816, doi: [10.1086/305774](https://doi.org/10.1086/305774)

- Hopkins, P. F., Hernquist, L., Cox, T. J., et al. 2005, *ApJ*, 630, 705, doi: [10.1086/432438](https://doi.org/10.1086/432438)
- Hopkins, P. F., Hernquist, L., Cox, T. J., & Kereš, D. 2008, *ApJS*, 175, 356, doi: [10.1086/524362](https://doi.org/10.1086/524362)
- Hwang, H.-C., Shen, Y., Zakamska, N., & Liu, X. 2020, *ApJ*, 888, 73, doi: [10.3847/1538-4357/ab5c1a](https://doi.org/10.3847/1538-4357/ab5c1a)
- Keeton, C. R. 2001, arXiv e-prints, astro, doi: [10.48550/arXiv.astro-ph/0102340](https://doi.org/10.48550/arXiv.astro-ph/0102340)
- Kim, D., Im, M., Glikman, E., Woo, J.-H., & Urrutia, T. 2015, *ApJ*, 812, 66, doi: [10.1088/0004-637X/812/1/66](https://doi.org/10.1088/0004-637X/812/1/66)
- Koss, M., Mushotzky, R., Treister, E., et al. 2012, *ApJL*, 746, L22, doi: [10.1088/2041-8205/746/2/L22](https://doi.org/10.1088/2041-8205/746/2/L22)
- Linford, J. 2022, *VLBA Scientific Memos*, 38
- Madau, P., & Dickinson, M. 2014, *ARA&A*, 52, 415, doi: [10.1146/annurev-astro-081811-125615](https://doi.org/10.1146/annurev-astro-081811-125615)
- Magorrian, J., Tremaine, S., Richstone, D., et al. 1998, *AJ*, 115, 2285, doi: [10.1086/300353](https://doi.org/10.1086/300353)
- Mangat, C. S., McKean, J. P., Brilenkov, R., et al. 2021, *MNRAS*, 508, L64, doi: [10.1093/mnrasl/slab106](https://doi.org/10.1093/mnrasl/slab106)
- Marconi, A., & Hunt, L. K. 2003, *ApJL*, 589, L21, doi: [10.1086/375804](https://doi.org/10.1086/375804)
- Müller-Sánchez, F., Comerford, J. M., Nevin, R., et al. 2015, *ApJ*, 813, 103, doi: [10.1088/0004-637X/813/2/103](https://doi.org/10.1088/0004-637X/813/2/103)
- Patnaik, A. R., Browne, I. W. A., King, L. J., et al. 1993, *MNRAS*, 261, 435, doi: [10.1093/mnras/261.2.435](https://doi.org/10.1093/mnras/261.2.435)
- Peng, C. Y., Ho, L. C., Impey, C. D., & Rix, H.-W. 2002, *AJ*, 124, 266, doi: [10.1086/340952](https://doi.org/10.1086/340952)
- Richards, G. T., Hall, P. B., Vanden Berk, D. E., et al. 2003, *AJ*, 126, 1131, doi: [10.1086/377014](https://doi.org/10.1086/377014)
- Richards, G. T., Lacy, M., Storrie-Lombardi, L. J., et al. 2006, *ApJS*, 166, 470, doi: [10.1086/506525](https://doi.org/10.1086/506525)
- Richards, G. T., Kruczek, N. E., Gallagher, S. C., et al. 2011, *AJ*, 141, 167, doi: [10.1088/0004-6256/141/5/167](https://doi.org/10.1088/0004-6256/141/5/167)
- Rodriguez-Gomez, V., Genel, S., Vogelsberger, M., et al. 2015, *MNRAS*, 449, 49, doi: [10.1093/mnras/stv264](https://doi.org/10.1093/mnras/stv264)
- Rubin, K. H. R., O’Meara, J. M., Cooksey, K. L., et al. 2018, *ApJ*, 859, 146, doi: [10.3847/1538-4357/aaaeb7](https://doi.org/10.3847/1538-4357/aaaeb7)
- Rubinur, K., Das, M., & Kharb, P. 2019, *MNRAS*, 484, 4933, doi: [10.1093/mnras/stz334](https://doi.org/10.1093/mnras/stz334)
- Sanders, D. B., Soifer, B. T., Elias, J. H., et al. 1988, *ApJ*, 325, 74, doi: [10.1086/165983](https://doi.org/10.1086/165983)
- Shen, Y., & Liu, X. 2012, *ApJ*, 753, 125, doi: [10.1088/0004-637X/753/2/125](https://doi.org/10.1088/0004-637X/753/2/125)
- Shen, Y., Richards, G. T., Strauss, M. A., et al. 2011, *ApJS*, 194, 45, doi: [10.1088/0067-0049/194/2/45](https://doi.org/10.1088/0067-0049/194/2/45)
- Shen, Y., Chen, Y.-C., Hwang, H.-C., et al. 2021, *Nature Astronomy*, 5, 569, doi: [10.1038/s41550-021-01323-1](https://doi.org/10.1038/s41550-021-01323-1)
- Shen, Y., Hwang, H.-C., Oguri, M., et al. 2023, *ApJ*, 943, 38, doi: [10.3847/1538-4357/aca662](https://doi.org/10.3847/1538-4357/aca662)
- Shields, G. A., Rosario, D. J., Junkkarinen, V., et al. 2012, *ApJ*, 744, 151, doi: [10.1088/0004-637X/744/2/151](https://doi.org/10.1088/0004-637X/744/2/151)
- Spingola, C., McKean, J. P., Lee, M., Deller, A., & Moldon, J. 2019, *MNRAS*, 483, 2125, doi: [10.1093/mnras/sty3189](https://doi.org/10.1093/mnras/sty3189)
- Steinborn, L. K., Dolag, K., Comerford, J. M., et al. 2016, *MNRAS*, 458, 1013, doi: [10.1093/mnras/stw316](https://doi.org/10.1093/mnras/stw316)
- Stocke, J. T., Morris, S. L., Weymann, R. J., & Foltz, C. B. 1992, *ApJ*, 396, 487, doi: [10.1086/171735](https://doi.org/10.1086/171735)
- Telfer, R. C., Zheng, W., Kriss, G. A., & Davidsen, A. F. 2002, *ApJ*, 565, 773
- Urrutia, T., Becker, R. H., White, R. L., et al. 2009, *ApJ*, 698, 1095, doi: [10.1088/0004-637X/698/2/1095](https://doi.org/10.1088/0004-637X/698/2/1095)
- Urrutia, T., Lacy, M., & Becker, R. H. 2008, *ApJ*, 674, 80, doi: [10.1086/523959](https://doi.org/10.1086/523959)
- Urrutia, T., Lacy, M., Spoon, H., et al. 2012, *ApJ*, 757, 125, doi: [10.1088/0004-637X/757/2/125](https://doi.org/10.1088/0004-637X/757/2/125)
- Van Wassenhove, S., Volonteri, M., Mayer, L., et al. 2012, *ApJL*, 748, L7, doi: [10.1088/2041-8205/748/1/L7](https://doi.org/10.1088/2041-8205/748/1/L7)
- Vestergaard, M., & Wilkes, B. J. 2001, *ApJS*, 134, 1, doi: [10.1086/320357](https://doi.org/10.1086/320357)
- Wilson, J. C., Henderson, C. P., Herter, T. L., et al. 2004, in *Proc. SPIE*, Vol. 5492, Ground-based Instrumentation for Astronomy, ed. A. F. M. Moorwood & M. Iye, 1295–1305, doi: [10.1117/12.550925](https://doi.org/10.1117/12.550925)
- Yue, M., Fan, X., Yang, J., & Wang, F. 2021, *ApJL*, 921, L27, doi: [10.3847/2041-8213/ac31a9](https://doi.org/10.3847/2041-8213/ac31a9)